



# Exergetic, exergoeconomic, and exergoenvironmental assessments and optimization of a novel solar cascade organic Rankine cycle-assisted hydrogen liquefaction

F. Ahmadi Boyaghchi\* and A. Sohbatloo

*Department of Mechanical Engineering, Faculty of Engineering, Alzahra University, Tehran, Iran.*

Received 28 February 2019; received in revised form 30 May 2019; accepted 23 September 2019

## KEYWORDS

Linear fresnel solar collector;  
 Cascade organic rankine cycle;  
 Exergoeconomic analysis;  
 Exergoenvironmental analysis;  
 Mixed refrigerant;  
 Optimization.

**Abstract.** In this research, a combination of Cascade Organic Rankine Cycle (CORC) and ejector refrigeration loops incorporated with the concentrating Linear Fresnel Solar Collector (LFSC) is proposed as a pre-cooling system to reduce electricity consumption in the Mixed Refrigerant (MR) hydrogen liquefaction process. Exergetic, exergoeconomic, and exergoenvironmental analyses of the system over a year and on particular days were conducted in detail. Moreover, the annual thermodynamic, economic, and Environmental Impact (EI) performances of the proposed system were evaluated by varying the substantial design parameters. Parametric study indicated that increasing the back pressure of a turbine in the Low-Temperature (LT) loop would improve all of the aforementioned system performances. Meanwhile, bi-objective optimization based on Non-dominated Sorting Genetic Algorithm (NSGA-II) and LINMAP, TOPSIS and Shannon entropy decision-makers were used to ascertain the optimum  $COP_{Ex}$  and economic/EI factors of the system. According to the results,  $COP_{Ex}$  was enhanced by 10% and the cost and EI per exergy unit of  $LH_2$  were reduced to 0.0309 \$/MJ and 1.361 Pts/MJ using the TOPSIS method.

© 2021 Sharif University of Technology. All rights reserved.

## 1. Introduction

Integration of renewable energies, such as solar and geothermal energies, to improve industrial processes as well as application of sustainable energy sources are the most effective ways to mitigate the environmental contamination problems related to utility of power plants. One of the most important and sustainable energy sources is hydrogen ( $H_2$ ) energy and it is

expected to become an energy carrier for sustainable development in the future [1]. The gaseous state of  $H_2$  has lower energy content by volume. This energy content can be increased through liquefaction of  $H_2$ .

Attempts have been made to design and develop more effective cycles to liquefy  $H_2$  [2,3] and several methods have been proposed to increase the cooling efficiency of the  $H_2$  liquefaction process; for instance, an Mixed Refrigerant (MR) refrigeration cycle with various refrigerants has been proposed as a pre-cooling cycle to pre-cool  $H_2$  from 25°C to -193°C [2,4–8]. Utilizing the cold energy of Liquefied Natural Gas (LNG) in the regasification process is another way to pre-cool  $H_2$  [9].

The  $H_2$  liquefaction process can be integrated with a renewable energy-driven system to reduce en-

\*. Corresponding author. Tel.: +98 21 88044040;  
 Fax: +98 21 88617537  
 E-mail address: fahmadi@alzahra.ac.ir (F. Ahmadi Boyaghchi)

ergy consumption and make the process more sustainable [10]. In this respect, Kanoglu et al. [10] studied three scenarios concerning the use of geothermal energy for  $H_2$  liquefaction. They considered a binary cycle for a geothermal power plant and a pre-cooled Linde-Hampson cycle for the liquefaction of  $H_2$ . They found that pre-cooling  $H_2$  had a considerable energy saving potential in the  $H_2$  liquefaction process. Gadalla et al. [11] used a triple-effect absorption refrigeration cycle as a pre-cooler in the Linde-Hampson  $H_2$  liquefaction cycle. They investigated energy- and exergy-based performances of the cycle by varying the major design parameters and found that both  $COP_{En}$  and  $COP_{Ex}$  decreased from 1.33 to 0.12 and 0.92 to 0.08, respectively, upon an increase in the mass flow rate of geothermal water. Kanoglu et al. [12] proposed a geothermally driven ammonia-water absorption refrigeration cycle as a pre-cooler for the Claude  $H_2$  liquefaction cycle. In the proposed cycle,  $H_2$  cooled down to  $-26.9^\circ\text{C}$ . In addition,  $COP_{En}$  in the absorption section and  $COP_{Ex}$  in the entire cycle were determined as 0.162 and 0.679, respectively. Yilmaz [13] proposed a geothermal water-ammonia absorption pre-cooler for Claude  $H_2$  liquefaction unit. The proposed system was analyzed based on exergoeconomic concept. Moreover, the exergoeconomic optimization procedure was conducted to obtain the minimum cost rate for the system. The results showed that  $H_2$  gas could be cooled down to  $-30^\circ\text{C}$  in the pre-cooling cycle and the unit exergetic liquefaction cost of  $H_2$  was calculated as 9.27 \$/GJ in the optimum case. Aasadnia and Mehrpooya [14] presented a solar-driven absorption refrigeration cycle to enhance a pre-cooler MR refrigeration cycle, which was coupled with Joule-Brayton cryogenic section. In this design, some  $H_2$  streams in the pre-cooling and cryogenic sections were cooled by the solar absorption section. Energy, exergy, and economic analyses were conducted for the proposed system. According to the results, the  $H_2$  gas was cooled down to  $-25^\circ\text{C}$  via solar absorption section.  $COP_{En}$  and  $COP_{Ex}$  of the proposed system were 0.2034 and 0.455, respectively.

In addition to absorption refrigeration cycles, Organic Rankine Cycles (ORCs) operate at low temperatures due to the low boiling point of organic fluids. The superiority of these cycles to produce power has been demonstrated by several researchers [15–17]. For this purpose, Kaşka et al. [18] proposed an organic Rankine-vapor compression cycle driven by geothermal energy to pre-cool  $H_2$  gas for Claude  $H_2$  liquefaction cycle and analyzed the proposed system using the thermoeconomic concept. The results showed that  $H_2$  gas would enter the liquefaction cycle at about  $-40^\circ\text{C}$  without any additional work consumption. Moreover, liquefaction cost was calculated as 0.995 \$/(kg  $LH_2$ ) and the electricity produced by itself was calculated as 0.025 \$/kWh.

To the best of our knowledge and based on a survey of the mentioned literature review, a solar-driven Cascade Organic Rankine Cycle (CORC) equipped with ejector refrigeration loops to pre-cool  $H_2$  and produce power simultaneously at the  $H_2$  liquefaction plant has not been performed so far. The novelty of this work is to design and integrate a new solar-driven CORC equipped with ejector with an MR cryogenic liquefaction section for the first time in order to achieve a lower temperature for pre-cooling  $H_2$ . Linear Fresnel Solar Collector (LFSC) is selected to provide the required thermal energy for CORC due to its simpler configuration and lower maintenance and operation costs than parabolic trough collectors [19–22]. The major objectives established in this work are:

- To propose a novel solar-driven  $H_2$  liquefaction cycle;
- To demonstrate the advantages of the proposed pre-cooler over those of other pre-coolers presented in the literature;
- To analyze the proposed system using energy, exergy, and exergoeconomic and exergoenvironmental concepts;
- To predict the energy- and exergy-based performances of the system during solstices, equinoxes, and a year;
- To study the effect of the major design operating conditions on the energy- and exergy-based performances of the cycle;
- To optimize the exergetic and cost/EI performances of the system using an evolutionary algorithm based on NSGA-II;
- To ascertain the final optimum operation of the system using LINMAP, TOPSIS, and Shannon entropy decision-making.

## 2. System description and assumptions

A schematic diagram of the proposed  $H_2$  liquefaction plant is shown in Figure 1. The system is a combination of three major subsystems, namely solar CORC pre-cooling, MR cryogenics, and liquefying sections. Solar CORC consists of an LFSC field, three thermal storage tanks, and two High-Temperature (HT) and Low-Temperature (LT) ORCs equipped with two ejector refrigeration loops. R32 and R116 with critical temperatures of  $78.1^\circ\text{C}$  and  $19.88^\circ\text{C}$  [23] are used as organic working fluids inside HT and LT ORCs, respectively. These zero ozone depletion potential fluids are selected in order to achieve temperature matching, high system efficiency, safety operation, and minimal environment impact in the system [24,25].

In this section, LFSC field provides the required thermal energy of CORC over a day by increasing the

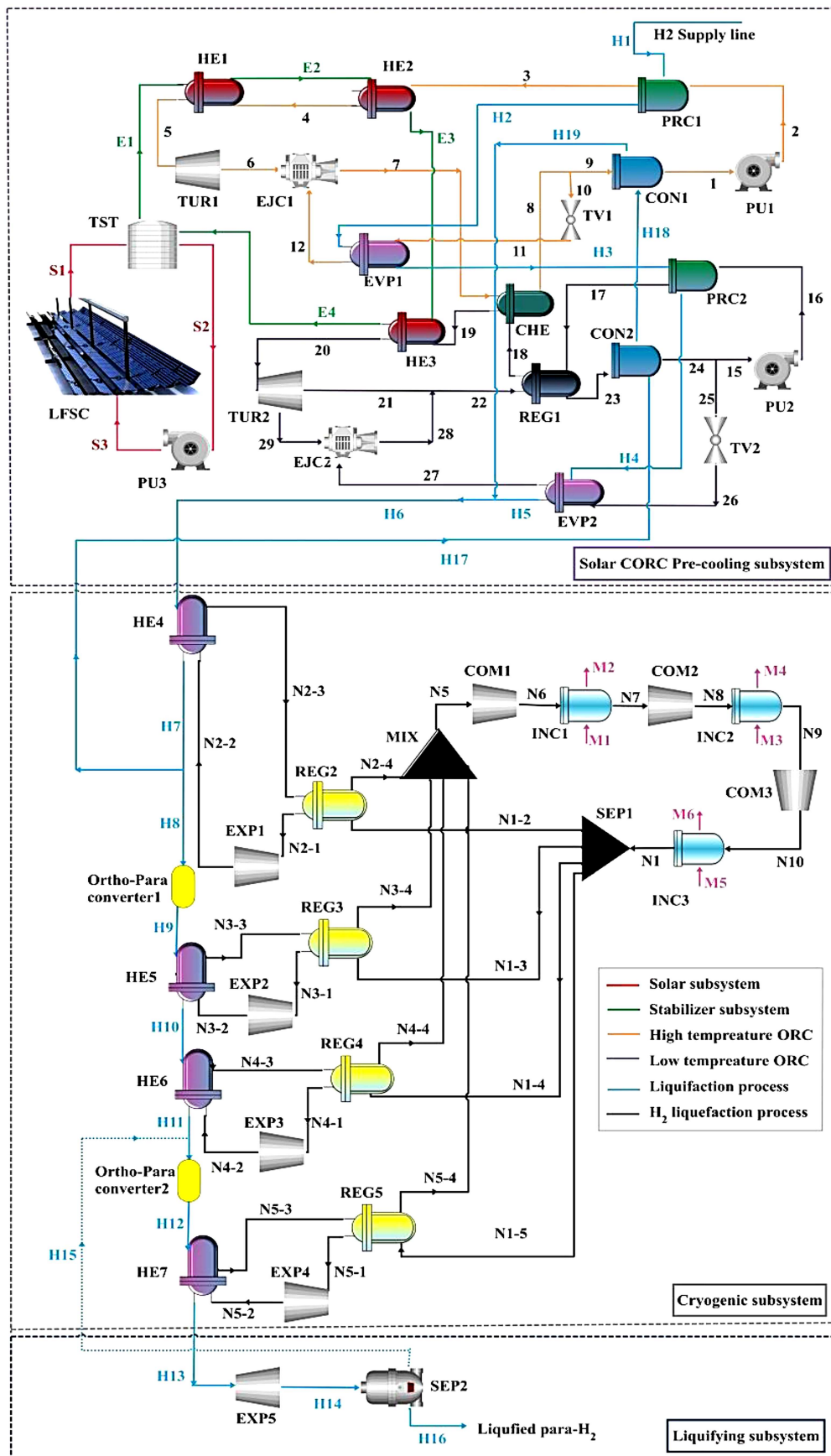


Figure 1. Process flow diagram of the proposed H<sub>2</sub> liquefaction cycle.

internal energy of Therminol VP-1 in Thermal Storage Tank (TST). In HT cycle, the saturated R32 with a low temperature (stream 1) is pressurized in PU1 (stream 2) and preheated (stream 3) by receiving heat from the H<sub>2</sub> feed stream in PRC1 (streams H1 and H2). Then, it enters HE2 and HE1 to be superheated (streams 4 and 5) by absorbing heat from Therminol VP-1 circulating inside the stabilizing subsystems (streams E1, E2, and E3). The stream discharged from HE1 flows into TUR1 to produce power. The expanded stream (stream 6) then flows into EJC1 as a primary flow. The pressure of the primary stream drastically declines at the exit of nozzle and sucks the throttled secondary flow leaving EVP1 (stream 12). The cooling load produced in EVP1 by throttling a portion of the stream discharged from Cascade Heat Exchanger (CHE) (streams 10, 11 and 12) cools H<sub>2</sub> (stream H3). Then, the primary and secondary flows mix at constant pressure in the mixing section of EJC1. The mixed stream passes through the diffuser section in which its pressure increases and then, leaves EJC1 (Stream 7). The remaining stream flowing into CON1 (stream 9) is cooled by a branch of H<sub>2</sub> extracted from a stream in the cryogenic cycle (streams H18 and H19). In the LT cycle, the pressurized R116 (stream 16) is preheated in PRC2 (stream 17) by absorbing the heat from the H<sub>2</sub> feed stream leaving EVP1 (stream H3) and then, it is heated when passing through REG1, CHE, and HE3 (streams 18, 19, and 20). Then, the superheated stream flows into TUR2 to produce power. A portion of the stream is extracted (stream 29) as a primary flow in EJC2 and its pressure reduces at the exit of nozzle to provide the suction region for the throttled secondary stream from EVP2 (stream 27). The cooling capacity produced in EVP2 is utilized for cooling H<sub>2</sub> (streams H4 and H5). In EJC2, the two mixed streams exit (stream 28) and mix with the remaining flow leaving TUR2 (stream 21). This stream (stream 22) is pre-cooled in REG and turns into saturated liquid (Stream 23) by rejecting heat to H<sub>2</sub> (stream H17) in CON2. The cold H<sub>2</sub> is then fed to the cryogenic cycle (stream H6). In the MR cryogenic cycle, Ne, H<sub>2</sub>, and He with 10%, 6.5%, and 83.5% mole fractions are used as MR which is compressed in COMs 1 to 3. Next, it flows and is cooled into INCs 1 to 3 as streams N6, N8, and N10. The high-pressure refrigerant of N1 is divided into four streams, i.e., N1-2, N1-3, N1-4, and N1-5, and they are cooled in REG2, REG3, REG4, and REG5, respectively, by rejecting heat to the returned streams. Then, they flow into EXPs 1 to 4 to expand to lower temperatures and pressures and provide refrigeration load in HEs 4 to 7 to cool H<sub>2</sub> stream. A portion of H<sub>2</sub> stream leaving HE4 is extracted to cool the working fluids in CON1 and CON2 and the remaining stream is fed to the ortho-para converter 1 (streams H8 and H9) to be converted to para-H<sub>2</sub> with a concentration of

70%. The concentration of para-H<sub>2</sub> increases up to 99% passing through the ortho-para converter 2 (streams H11 and H12). The feed stream exiting HE7 (stream H13) is expanded in EXP5 to produce a low-quality mixture (stream H14). The liquid fraction of para-H<sub>2</sub> is separated in SEP (stream H16) and the gas fraction returns to the cycle.

The following assumptions are applied to simplify the present study:

- All components operate in steady state conditions;
- Kinetic and potential energies for each component are neglected;
- The ambient temperature and pressure are considered 25°C and 101.3 kPa, respectively;
- The pressure drops in pipes due to the frictional losses are neglected;
- The working fluids leaving the condenser and evaporator are saturated liquid and saturated vapor, respectively;
- TST is assumed to be insulated and the unsteady well-mixed model is used to estimate the temperature of Therminol VP-1 during a day [26];
- Ejector is modeled using the correlations based on the one-dimensional constant pressure flow presented by Li et al. [27];
- All valves operate isenthalpically.

### 3. Energy analysis

Mass and energy balances are applied for each component according to the assumptions made in Section 2 and the energy model of LFSC is conducted using the relations expressed in the following section.

#### 3.1. LFSC simulation

The desired LFSC in this work consists of many flat mirrors as the first reflectors, a tubular receiver enveloped by the vacuumed glass tube, and a parabolic cavity as the second reflector [28]. The total solar energy received by LFSC is given as follows [29]:

$$\dot{Q}_{Sun} = G_B A_{ap}, \quad (1)$$

where  $G_B$  indicates the beam radiation falling on the horizontal surface and  $A_{ap}$  is the LFSC aperture area given by [29]:

$$A_{ap} = 2L \sum_{i=1}^n w \cos \theta_n. \quad (2)$$

In Eq. (2),  $L$  and  $w$  are the length and width of the constituent mirror elements, respectively,  $\theta_n$  is the tilt angle of mirrors, and  $n$  is the number of mirrors.

The heat absorbed by the receiver can be obtained as follows [29]:

$$S = G_B \gamma_1 \gamma_2 \tau \alpha r. \tag{3}$$

Here,  $\gamma_1$  and  $\gamma_2$  indicate the relectivity of the first and second parabolic relectors, respectively,  $\tau$  is the glas envelope transitivity,  $\alpha$  is the absorber absorptivirty, and  $r$  is the shading factor.

The useful heat gain by Therminol VP-1 passing through the receiver can be calculated by [29]:

$$\begin{aligned} \dot{Q}_u &= A_r \left[ S - \frac{U_L}{C} (T_r - T_a) \right] \\ &= \dot{m} C_P (T_{outlet} - T_{inlet}). \end{aligned} \tag{4}$$

In Eq. (4),  $A_r$  is the receiver area,  $C$  is the concentration ratio,  $\dot{m}$  is the mass flow rate,  $C_p$  is the specific heat, and  $T$  is the temperature. The indexes “ $r$ ” and “ $a$ ” refer to the receiver and air, respectively. The  $U_L$  presented in Eq. (4) indicates the overall heat loss coefficient [29,30]:

$$U_L = \left[ \frac{1}{\lambda_{r,r-g}} + \frac{1}{\lambda_{c,g-g}} + \frac{D_{o,r}}{(\lambda_{c,g-a} + \lambda_{r,g-a}) D_{i,g}} \right]^{-1}. \tag{5}$$

In Eq. (5),  $D$  refers to the diameter,  $\lambda_{r,r-g}$  is the radiation heat transfer coefficient between receiver and glass,  $\lambda_{c,g-g}$  is the conduction heat transfer coefficient within glass wall,  $\lambda_{c,g-a}$  is the convection heat transfer coefficient by wind, and  $\lambda_{r,g-a}$  is the radiation heat transfer coefficient between glass and air. The aforementioned heat transfer coefficients can be calculated using the correlations in [29,30].

The pressure loss ( $\Delta P_f$ ) of Therminol-VP1 through the receiver tube in each LFSC segment is determined through the subsequent equation [29]:

$$\Delta P_f = \frac{L f V_f^2 \rho_f}{2 D_{i,r}}, \tag{6}$$

where  $f$  is the coefficient of friction and  $\rho$  is density. The flow coefficients of friction for laminar and turbulent flows are calculated using Eqs. (7) and (8), respectively [29,30]:

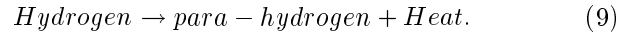
$$f = \frac{16}{Re_f}, \tag{7}$$

$$f = 0.0791(Re)^{-0.25}. \tag{8}$$

### 3.2. Ortho-para hydrogen conversion

Hydrogen is created through a combination of two nuclear spins of the atoms, called ortho-hydrogen and para-hydrogen; this combination is a function of temperature only. The nuclear spins of para-hydrogen are antiparallel, whereas the nuclear spins of ortho-hydrogen are parallel. At ambient temperature, the percentage of hydrogen composition becomes nearly

75% ortho-hydrogen and 25% para-hydrogen [3]. The equilibrium ratio of ortho-hydrogen to para-hydrogen at the normal boiling point is 0.2%; however, non-catalytic conversion from ortho to para has a very slow rate. Therefore, if hydrogen liquefaction is carried out without an ortho-para catalytic conversion, the ortho state will have much more concentration than its equilibrium concentration and it will be converted spontaneously to the para state [14]. The conversion reaction of the ortho-para conversion is set as follows [3]:



### 4. Exergy analysis

Unlike the energy analysis, exergy analysis is a convenient tool to identify the type and magnitude of thermodynamic irreversibilities and the exergy loss due to the exergy transfer to the environment within each component of the energy system. The exergy balance equation for a control volume can be described as follows [30]:

$$\dot{E}x_Q + \sum_{inlet} \dot{E}x_{inlet} = \dot{E}x_W + \sum_{outlet} \dot{E}x_{outlet} + \dot{E}x_D. \tag{10}$$

Here,  $\dot{E}x_D$  is the total exergy destruction and  $\dot{E}x_Q$  is the exergy flow related to the heat transfer through the control volume boundaries and is given below [30,31]:

$$\dot{E}x_Q = \dot{Q} \left( 1 - \frac{T_0}{T} \right). \tag{11}$$

$\dot{E}x_W$  is the exergy rate associated with the work which is calculated as follows [30,31]:

$$\dot{E}x_W = \dot{W}. \tag{12}$$

In Eq. (10),  $\dot{E}x$  is the stream exergy. The subscripts “inlet” and “outlet” refer to the entering and outgoing streams of matter and are defined by [30,31]:

$$\dot{E}x = \dot{m}.ex, \tag{13}$$

where  $ex$  is the sum of the chemical exergy and physical exergy described as follows [30,31]:

$$ex^{Ph} = (h - h_0) - T_0 (s - s_0). \tag{14}$$

Here,  $h$  and  $s$  are the enthalpy and entropy. For each stream with a temperature lower than the reference temperature  $T_0$ , the physical exergy  $ex^{Ph}$  can be divided into the thermal ( $ex^T$ ) and mechanical ( $ex^M$ ) exergy components as follows [31]:

$$\begin{aligned} ex^{Ph} &= \underbrace{[(h - h_x) - T_0 (s - s_x)]_{P=const}}_{ex^T} \\ &+ \underbrace{[(h_x - h_0) - T_0 (s_x - s_0)]_{T_0=const}}_{ex^M}, \end{aligned} \tag{15}$$

where the point  $x(T_0, P)$  is defined at the given pressure  $P$  of each stream and the temperature  $T_0$  of the environment.

The specific chemical exergy of the stream can be calculated as follows [31]:

$$ex^{ch} = \frac{1}{M} \left[ \sum y_i (\xi_i^0 - \xi_i^{00}) \right], \tag{16}$$

where  $\xi_i^0$  is the chemical potential of the  $i$ th component in the restricted dead state,  $\xi_i^{00}$  is the chemical potential of the  $i$ th component in the chemical equilibrium,  $y_i$  is the molar fraction of the  $i$ th component, and  $M$  is the molecular mass. Eq. (10) can be categorized to fuel-product-loss exergies for each component [30]. Then, the exergy efficiency of each component can be determined as follows [30,31]:

$$\eta_{Ex} = \frac{\dot{E}x_P}{\dot{E}x_F}. \tag{17}$$

Exergoeconomic analysis is carried out to compute the cost per unit exergy of the streams by revealing the cost formation processes. In the present work, the Specific Exergy Costing (SPECO) approach is adopted due to its straightforward scheme and efficient calculation [32]. The related cost balance equation for each component of the energy system is defined as follows [30]:

$$\dot{C}_Q + \sum_{inlet} \dot{C}_{inlet} + \dot{Z} = \sum_{outlet} \dot{C}_{outlet} + \dot{C}_W, \tag{18}$$

where  $\dot{C}_Q$  and  $\dot{C}_W$  are the costs of heat transfer and work and can be calculated as follows [30]:

$$\dot{C}_Q = c_Q \cdot \dot{E}x_Q, \tag{19}$$

$$\dot{C}_W = c_W \cdot \dot{E}x_W. \tag{20}$$

Here,  $\dot{C}_{inlet}$  and  $\dot{C}_{outlet}$  are the costs of entering and exiting streams of matter containing  $\dot{C}^{Ph}$  and  $\dot{C}^{ch}$  parts [30]:

$$\dot{C} = c \cdot \dot{E}x. \tag{21}$$

In Eqs. (19) to (21),  $c$  denotes the average costs per unit of exergy. The  $\dot{Z}$  appears in Eq. (18) and is the total cost rate of capital investment, which is the sum of the cost rates associated with capital investment ( $\dot{Z}^{CI}$ ) and operations and maintenance ( $\dot{Z}^{OM}$ ). The value of  $\dot{Z}$  is calculated as follows [30]:

$$\dot{Z} = \frac{Z \times \varphi \times CRF}{N}. \tag{22}$$

Here,  $Z$  is the purchase cost of each component expressed in [33–36],  $\varphi$  is the maintenance factor (i.e., 1.06), and CRF refers to the capital recovery factor being expressed by [30]:

$$CRF = \frac{i_r(1 + i_r)^N}{(1 + i_r)^N - 1}. \tag{23}$$

In Eq. (23),  $i_r$  is the interest rate (i.e., 10%) and  $N$  refers to the system life (i.e., 25 years and 7446 working hours per year at full capacity).

Exergy destruction cost rate for each component can be calculated as follows [30]:

$$\dot{C}_D = c_F \dot{E}x_D, \tag{24}$$

where  $c_F$  is the average cost per unit exergy of fuel for each component and can be calculated as follows [30]:

$$c_F = \frac{\dot{C}_F}{\dot{E}x_F}. \tag{25}$$

Exergoeconomic factor ( $f_c$ ) and relative cost difference ( $r_c$ ) are defined as follows [30]:

$$f_c = \frac{\dot{Z}}{\dot{Z} + \dot{C}_D}, \tag{26}$$

$$r_c = \frac{c_P - c_F}{c_F}, \tag{27}$$

where  $c_P$  denotes the average cost per unit exergy of the product within each component and calculated as follows [30]:

$$c_P = \frac{\dot{C}_P}{\dot{E}x_P}. \tag{28}$$

The cost balance and cost rates per unit of exergy are calculated using an additional auxiliary equation based on Fuel-Product rules, and the cost of electricity required for compressors is set to 0.08 \$/kWh.

Exergoenvironmental analysis is a combination of the exergy concept and Life Cycle Assessment (LCA). LCA is used to evaluate the Environmental Impact (EI) related to a component ( $Y$ ) over its lifetime and it is assessed here using ECO-indicator 99 [37]. The value of  $Y$  for each device of energy system can be calculated using Eq. (34):

$$Y = \sum_i m_i \omega_i. \tag{29}$$

Here,  $m$  is the mass of constituent materials of each component and  $\omega$  is the life cycle inventory associated with the production, which can be obtained from LCA and ECO-indicator 99 [38,39].

Meanwhile, the average EI per exergy unit ( $b$ ) associated with the production of each stream can be calculated using the environmental balance for a component and auxiliary equations based on the Fuel and Product rules. The exergoenvironmental balance for a component is formulated as follows [37]:

$$\dot{B}_Q + \sum_{inlet} \dot{B}_{inlet} + (\dot{Y} + \dot{B}^{PF}) = \sum_{outlet} \dot{B}_{outlet} + \dot{B}_W. \quad (30)$$

Here,  $\dot{B}$  ( $= b\dot{E}x$ ) is the EI rate associated with exergy consisting of  $\dot{B}^{Ph}$  and  $\dot{B}^{ch}$  parts. The EI rates associated with heat and work transfers are calculated as follows [37]:

$$\dot{B}_Q = b \times \dot{E}x_Q, \quad (31)$$

$$\dot{B}_W = b \times \dot{W}. \quad (32)$$

The subscripts “inlet” and “outlet” refer to entering and exiting streams and  $\dot{Y}$  ( $= Y/N$ ) is the component-related EI rate.  $\dot{B}^{PF}$  is the EI of pollutant formation within the component and it is considered only when a chemical reaction takes place; otherwise, it is zero. The value of EI related to the electricity is set to 27 mPts/kWh [40]. Meanwhile, to evaluate the EI of each component, environmental variables are stated as follows [37,41]:

$$b_F = \frac{\dot{B}_F}{\dot{E}x_F}, \quad (33)$$

$$b_P = \frac{\dot{B}_P}{\dot{E}x_P}. \quad (34)$$

In Eqs. (33) and (34),  $b_F$  and  $b_P$  refer to the EI per exergy unit of the fuel and the product related to each component, respectively.

$$\dot{B}_D = b_F \dot{E}x_D, \quad (35)$$

where  $\dot{B}_D$  is the EI of exergy destruction rate. The exergoenvironmental factor ( $f_b$ ) and the relative EI difference ( $r_b$ ) are defined as follows [37,41]:

$$f_b = \frac{\dot{Y}}{\dot{Y} + \dot{B}_D}, \quad (36)$$

$$r_b = \frac{b_F - b_P}{b_F}. \quad (37)$$

### 5. Performance evaluation

$COP_{En}$  for the proposed system is defined as the ratio of cooling capacity for liquefaction of  $H_2$  to the cycle input energies including the solar energy received by LFSC and net consumed power by compressors. Due to the fluctuant nature of the solar energy, the average annual performances are defined as follows:

$$COP_{En} = \frac{\dot{m}_{H1}h_{H1} + \dot{m}_{H16}h_{H16}}{Q_{Sun} + \dot{W}_{net}}, \quad (38)$$

$$\dot{W}_{net} = \sum_{k=1}^3 \dot{W}_{COMs} - \sum_{k=1}^2 \dot{W}_{TURs} - \sum_{k=1}^5 \dot{W}_{EXPs}. \quad (39)$$

The  $COP_{Ex}$  of the system is defined as the ratio of  $H_2$  thermal exergy difference to input exergies including  $H_2$  mechanical exergy difference, exergy of the sun, and the net power consumed by the compressors [42]:

$$COP_{Ex} = \frac{\dot{E}x_{H16}^T - \dot{E}x_{H1}^T}{(\dot{E}x_{H16}^M - \dot{E}x_{H1}^M) + \dot{E}x_{Sun} + \dot{W}_{net}}. \quad (40)$$

Here,  $\dot{E}x_{Sun}$  is the solar radiation exergy [43].

The product cost and EI rates of the proposed system are defined by Eqs. (41) and (42):

$$\dot{C}_P = c_{LH_2} \dot{E}x_{LH_2}, \quad (41)$$

$$\dot{B}_P = b_{LH_2} \dot{E}x_{LH_2}. \quad (42)$$

### 6. Multi-objective optimization

In this investigation, NSGA-II based on genetic algorithm proposed by Deb et al. [44] is used for multi-objective optimization. The flowchart of the genetic algorithm is given in Figure 2. In this algorithm, first, various individuals (design parameters) are defined casually as a primary population. According to the conformity between the objective functions, some of these individuals are chosen as parents to reproduce the next generation. Amalgamation of the chromosomes called parents to generate new population is accomplished by the crossover operator. Considering the point that selecting parents in order to produce a new generation is based on the fitness with respect to the objective functions, the generation compatibility will

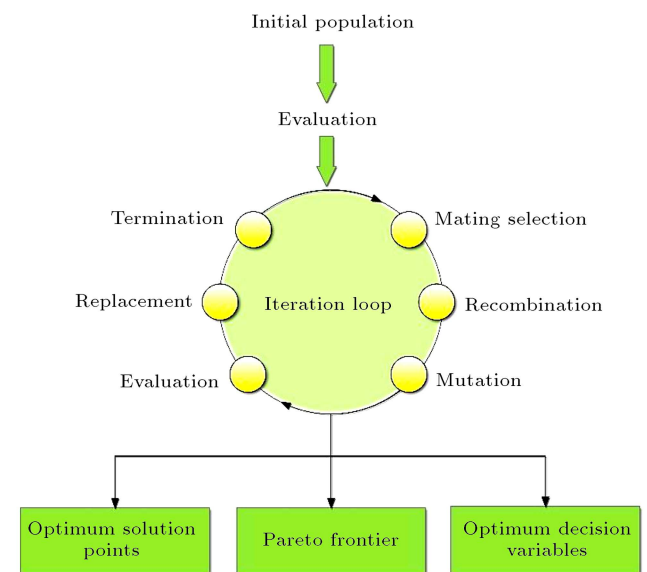


Figure 2. Genetic algorithm flow chart.

be improved step by step [45,46]. In multi-objective problems, decision-making is required to select the final optimal solution from the Pareto frontier. In this study, three recognized decision-makers called LINMAP, TOPSIS, and Shannon entropy were used [47] to ascertain the final solution points.

### 7. Validation

The combined cooling and power CORC introduced in the solar subsystem is a developed layout of CORC proposed by Xue et al. [24], which is composed of only two ORCs to produce power. In the first step, a mathematical model is developed using Engineering Equation Solver (EES) software to simulate CORC in the same given conditions expressed in [24]. As presented in Table 1, good agreement can be observed between the results obtained from the present work

and those reported by Xue et al. [24]. Moreover, verification of MR cryogenic subsystem modeling is present in Table 2 by comparing the H<sub>2</sub> temperatures between the present outcomes and available numerical results concluded by Sadaghiani and Mehrpooya [2]. Obviously, the results of the present study fit well with available outcomes.

### 8. Results and discussion

The proposed system was comprehensively analyzed from energy, exergy, exergoeconomic, and EI viewpoints. The EES software was used to extract the refrigerant properties and calculate the correlative equations expressed in Section 5. Accordingly, the input values for the main design parameters as the base case are listed in Table 3. Meanwhile, south of Iran with 29° 36' N, 52° 32' E and annual solar irradiation

**Table 1.** Verification of the modeling of Cascade Organic Rankine Cycle (CORC) and Mixed Refrigerant (MR) cryogenic subsystems.

Parameter	CORC subsystem		
	Xue et al. [24]	Present work	Difference (%)
Total output power, $\dot{W}$ (kW)	1776.44	1870	5.2
Energy efficiency, $\eta_{E_n}$ (%)	25.64	25.82	0.7
Exergetic efficiency, $\eta_{E_x}$ (%)	31.02	32.3	4.12
Parameter	MR cryogenic subsystem		
	Sadaghiani and Mehrpooya [2]	Present work	Difference (%)
$T_{H9}$ (°C)	-195	-195	0
$T_{H10}$ (°C)	-220	-224	1.8
$T_{H11}$ (°C)	-240	-239.7	0.1
$T_{H13}$ (°C)	-253	-252.5	0.2

**Table 2.** The results obtained at the design point.

Performance	Value
Net consumed power, $\dot{W}$ (kWh)	10.26 <sup>a</sup>
Energetic coefficient of performance, $COP_{E_n}$	0.05
Exergetic coefficient of performance, $COP_{E_x}$	0.10
Cost rate of LH <sub>2</sub> , $\dot{C}_{LH_2}$ (\$/s)	2.197
EI rate of LH <sub>2</sub> , $\dot{B}_{LH_2}$ (Pts/s)	87.20
Mass flow rate of LH <sub>2</sub> , $\dot{m}_{LH_2}$ (kg/s)	0.473 99% Para H <sub>2</sub>
Cost per unit exergy of LH <sub>2</sub> , $c_{LH_2}$ (\$/MJ)	0.0363
EI per unit exergy of LH <sub>2</sub> , $b_{LH_2}$ (Pts/MJ)	1.44
Cost of LH <sub>2</sub> , $C_{LH_2}$ (\$/kg LH <sub>2</sub> )	4.65
EI of LH <sub>2</sub> , $B_{LH_2}$ (Pts/kg LH <sub>2</sub> )	184.4
Temperature of pre-cooled H <sub>2</sub> , $T_{H6}$ (°C)	-148.8 <sup>b,c,d,e</sup>

<sup>a</sup> 25.65% improvement compared with the results reported in [13];

<sup>b</sup> 121.9°C lower than that obtained in [12]; <sup>c</sup> 123.8°C lower than that obtained in [14];

<sup>d</sup> 108.8°C lower than that obtained in [18]; <sup>e</sup> 118.8°C lower than that obtained in [13].

**Table 3.** Input values of the main parameters for simulation of the proposed system [2,24,29].

Parameter	Value	Parameter	Value
<b>Stabilizer subsystem</b>		<b>CORC subsystem</b>	
$L$ (m)	32.5	$P_5$ (kPa)	2000
$w$ (m)	0.5	$P_{20}$ (kPa)	1532
Number of modules	15	$P_6$ (kPa)	1300
$\gamma$	0.93	$P_{21}$ (kPa)	60
$\tau$	0.95	$P_{29}$ (kPa)	735.5
$\alpha$	0.95	$P_E$ (kPa)	101.325
$r$	0.98	$P_{28}$ (kPa)	60
$\dot{m}_{LFSC}$ (kg/s)	20	$P_{27}$ (kPa)	35
$P_{S3}$ (kPa)	500	$\dot{m}_1$ (kg/s)	2
<b>H<sub>2</sub> Line</b>		$\dot{m}_{LT}$ (kg/s)	11.32
$P_{H1}$ (kPa)	2009	$\dot{m}_E$ (kg/s)	20
$T_{H1}$ (°C)	27	$\eta_{is,PU}$ (%)	95
$\dot{m}_{H1}$ (kg/s)	0.517	$\eta_{is,TUR}$ (%)	85
$\dot{m}_{H17}$ (kg/s)	9		
<b>MR cryogenic subsystem</b>			
$T_{N1}$ (°C)	25	$P_{N2-2}$ (kPa)	119.6
$P_{N1}$ (kPa)	1005	$T_{M1}$ (°C)	25
$\dot{m}_{N1-2}$ (kg/s)	21	$P_{M1}$ (kPa)	101
$\dot{m}_{N1-3}$ (kg/s)	2	$\eta_{is,COM}$ (%)	90
$\dot{m}_{N1-4}$ (kg/s)	2	$\eta_{is,EXP}$ (%)	85
$\dot{m}_{N1-5}$ (kg/s)	2		

of 5.64 (kWh/m<sup>2</sup>.day) was considered for simulation of the system.

According to the results, COP<sub>En</sub> and COP<sub>Ex</sub> of the proposed system were calculated as 0.05 and 0.1, respectively. The reason for the small value of COP<sub>En</sub> is the low quality of solar energy as a source reservoir. Since the exergy of solar energy is lower than its energy, the value of COP<sub>Ex</sub> was estimated greater than COP<sub>En</sub>. As can be observed, the net consumed power to produce 0.473 kg LH<sub>2</sub> was about 10.26 kWh, showing a nearly 25.65% improvement compared with the geothermally driven H<sub>2</sub> liquefaction proposed by Yilmaz [13]. Meanwhile, the cost and EI of LH<sub>2</sub> were calculated as 4.65 \$/kg LH<sub>2</sub> and 184.4 Pts/kg LH<sub>2</sub>, respectively. It was found that the temperature of pre-cooled H<sub>2</sub> leaving the solar CORC reached about -148.8°C, which was 121.9°C, 123.8°C, 108.8°C, and 118.8°C lower than those expressed in [12–14,18], respectively. Therefore, the proposed solar pre-cooler

is more effective than renewable-based pre-coolers presented in the literature.

Table 4 indicates the results of the thermodynamic, economic, and EI analyses of the major components of the proposed system. It was found that the highest exergy destruction rate belonged to EXP1, which contributed 16.18% of the total exergy destruction rate of the proposed system. REG3 yielded the maximum exergy efficiency of 99.73%. The infinite values of  $r_c$  and  $r_b$  for LFSC showed the highest potential of the cost and EI reductions of this component. Moreover, the low values of  $f_c$  and  $f_b$  imply that the amount of the exergy destruction associated with cost and EI rate would hold dominance over investment expenditures and EI-related component rates. Therefore, replacing the components with more effective and expensive ones could improve the exergoeconomic and exergoenvironmental performances of the system. Meanwhile, the highest  $f_c$  and  $f_b$  with a value of 100

**Table 4.** Results of exergy, exergoeconomic, and exergoenvironmental analyses for major components.

Components	Exergetic analysis		Exergoeconomic analysis								Exergoenvironmental analysis					
	$\dot{E}x_D$ (kW)	$\eta_{E_s}$ (%)	$\dot{Z}$ (\$/h)	$c_F$ (\$/GJ)	$c_P$ (\$/GJ)	$\dot{C}_D$ (\$/h)	$\dot{Z} + \dot{C}$ (\$/h)	$r_c$	$f_c$ (%)	$\dot{Y}$ (Pts/s)	$\dot{B}_D$ (Pts/s)	$\dot{Y}_D + \dot{B}_D$ (Pts/s)	$b_F$ (Pts/GJ)	$b_P$ (Pts/GJ)	$r_b$	$f_b$ (%)
EXP1	78.34	0.6408	1657	1010	28.132	6.0923	22.04	3.13	0.6615	1860	1802	137.9	82.97	58.14	60.95	6032.0
REG2	2.58	0.8985	1010	9948	54.153	52.754	1.399	0.03	0.0150	1561	1561	82.97	81.75	0.445	98.53	5303.0
COM3	99.47	0.3735	10.3	7.50	5.7463	0.0303	5.716	93.07	5.386	420.1	29.13	12.77	2	391.0	72.81	4046.0
LFSC	100	$\infty$	0.403	0	390.3	0	390.3	100	$\infty$	22.82	0	6.536	0	22.82	20.97	3654.0
CON2	7.30	2.4970	5004	1431	4.9182	4.5592	0.359	0.01	2.497	373.3	373.3	113.8	32.55	0.020	19.88	3186.0
INC2	40.70	8.9550	10220	1026	4.0712	2.4142	1.657	12.90	10.28	814.7	709.6	945.2	83.78	105.1	10.05	2353.0
INC3	44.69	11.740	12500	981.4	3.3855	1.8725	1.513	15.60	13.91	656.1	553.7	1202	80.64	102.4	7.85	1908.0
COM1	67.76	0.0904	2368	2171	8.7872	2.8332	5.954	35.88	0.141	1128	722.9	175.6	153.9	404.6	91.71	1305.0
REG5	25.65	0.0350	1057	1021	1.7701	1.3161	0.454	0.14	0.0351	390.1	389.5	86.87	83.93	0.541	96.61	1289.0
COM2	99.85	0.0785	8.089	7.50	6.2912	0.0092	6.282	97.95	3.821	432.2	8.867	9.642	2	423.4	92.73	1232.0
CON1	12.70	4.0290	71.97	1431	1.3617	1.1887	0.173	0.01	4.03	97.35	97.34	163.7	32.55	0.000	19.88	830.7
INC1	60.75	2.5170	3864	1099	1.8519	0.7269	1.125	30.50	3.622	305.1	212.0	411.6	89.04	93.02	28.43	661.4
TST	76.34	0.7914	338.9	189.2	0.4781	0.1131	0.365	3.46	0.8198	31.73	30.63	25.89	14.23	1.099	55.81	598.0
EXP3	71.19	2.6520	3606	987.5	1.9834	0.5714	1.412	1.60	2.695	171.8	169.1	299.9	81.17	2.756	27.38	578.6
EXP4	69.78	2.6520	3860	1057	2.0236	0.6116	1.412	1.50	2.656	183.7	180.9	317.6	86.87	2.756	27.38	578.6
EXP2	78.56	1.5490	2515	986.6	2.6578	0.5698	2.088	2.46	1.588	172.8	168.6	209.8	81.09	4.255	39.24	577.5
HE3	10.65	0.6690	12960	7766	3.1829	2.8439	0.339	0.08	0.6695	246.1	245.9	311.4	186.5	0.184	59.92	366.2
HE6	17.45	0.2497	1234	987.5	0.4182	0.3452	0.073	0.15	0.25	102.3	102.1	101.5	81.17	0.149	80.02	349.6
Ortho para converter2	14.93	0.0052	1438	1430	0.5759	0.4899	0.086	8.51	0.0057	47.89	43.81	35.72	35.52	4.075	99.48	342.6
Ortho para converter1	15.10	0.0053	1439	1431	0.5697	0.4837	0.086	9.33	0.0059	43.68	39.60	32.74	32.55	4.075	99.47	338.0
HE5	25.66	0.2423	1226	986.6	0.4170	0.3100	0.107	0.13	0.2318	91.85	91.73	99.89	81.09	0.120	80.5	314.2
HE7	9.18	0.8615	1968	1057	0.3050	0.2770	0.028	0.09	0.8195	82.05	81.97	158.1	86.87	0.075	53.72	262.1
EJC1	0.00	1.7250	34480	12650	1.8811	1.8811	0.000	0.00	1.725	162.6	162.6	828.0	303.8	0.000	36.69	148.7
HE4	75.47	0.0283	1038	1010	0.7394	0.1814	0.558	2.98	0.0291	55.29	53.64	85.39	82.97	1.648	97.25	129.6
HE1	82.06	3.7480	1609	338.9	0.2206	0.0396	0.181	1.52	3.806	11.05	10.88	124.4	25.89	0.168	21.06	116.8
EJC2	0.00	2.0160	18490	61.33	0.6973	0.6973	0.000	0.00	2.016	62.71	62.71	462.1	153.3	0.000	33.16	113.7
REG4	80.57	0.0030	987.5	984.5	0.5635	0.1095	0.454	3.88	0.0031	33.71	32.4	81.17	80.91	1.307	99.7	111.2
EVP1	1.16	51.580	536400	10200	1.1177	1.1047	0.013	0.00	51.58	93.28	93.28	12580	239.3	0.001	1.90	108.3
REG3	81.46	0.0027	986.6	984	0.5095	0.0945	0.415	3.10	0.0028	28.85	27.95	81.09	80.86	0.895	99.73	96.0

was related to LFSC due to the zero values of exergy destruction associated with cost and EI rates.

Figure 3(a) and (b) show the effect of solar beam radiation on the performances of the proposed system over solstices (21th June and 21th December) and equinoxes (21th September and 21th March) in the south of Iran. According to the figures, during the daylight, solar energy constitutes the major input energy of the system. Therefore, the opposite trend was observed for COPs with varying solar radiations from sunrise to sunset. Since the solar exergy is lower than that of energy, the proposed system gives better exergetic performance. Based on the results, the lowest  $COP_{En}$  and  $COP_{Ex}$  were calculated as 0.047 and 0.096,

respectively, at solar noon over the summer solstice with the maximum solar beam radiation of 985.1  $W/m^2$ . Additionally,  $COP_{En}$  and  $COP_{Ex}$  remain nearly constant at 0.055 and 0.11, respectively, because the major portion of the compressors consuming power was provided by the grid electricity. Over the studied days,  $LH_2$  cost and EI rates varied slightly with solar variations and were calculated as almost 87  $\$/s$  and 2.2 Pts/s, because the properties of  $LH_2$  were strongly affected by the MR cryogenic subsystem and solar subsystem had a slight influence on the  $H_2$  properties.

The monthly average performances of the system are plotted in Figure 4. As solar irradiation increases, the thermodynamic performances of the system drop

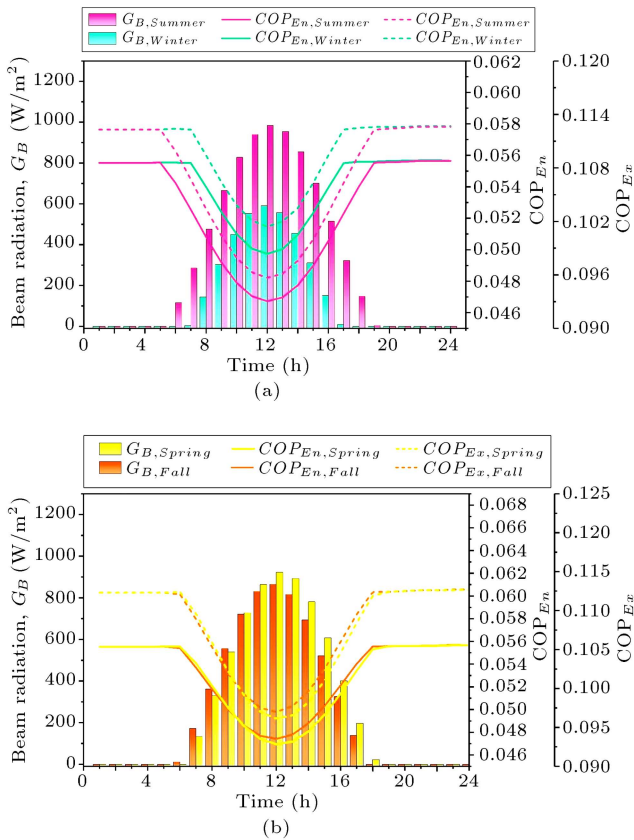


**Figure 3.** Hourly variation of COPs in (a) solstices (21th June and 21th December) and (b) equinoxes (21th September and 21th March) for south of Iran ( $27^{\circ}15' N$ ,  $59^{\circ}30' E$ ).

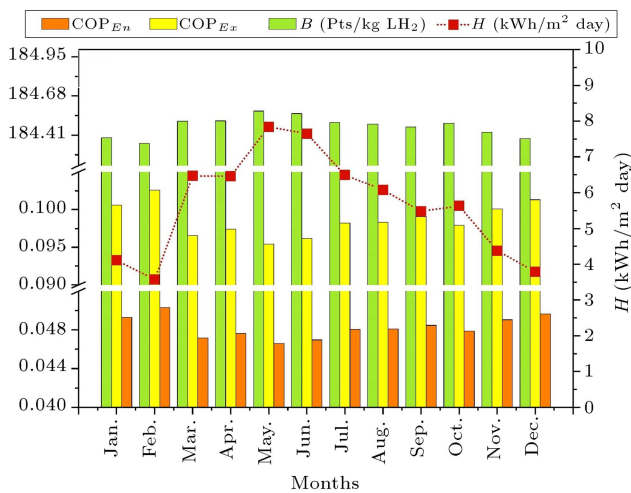


**Figure 4.** Monthly average performances of the proposed system.

due to the increase of compressors required power, although the produced power by turbines increases (about 3.23% during the first five months). Obviously, the maximum  $COP_{En}$  and  $COP_{Ex}$  were obtained as 0.05 and 0.103 with minimum solar radiations. The tendency of slight variations occurring in EI of  $LH_2$

stands in contrast to that for COPs because as solar radiation increases, the EI per unit of  $LH_2$  exergy grows. The minimum EI was obtained as 184.35 Pts/(kg  $LH_2$ ) for February.

### 8.1. Parametric study

In this section, a parametric assessment is conducted to evaluate the effect of the substantial design parameters, namely TUR1 inlet pressure ( $P_5$ ), TUR2 inlet and back pressures ( $P_{20}$  and  $P_{21}$ ), EJC2 primary pressure ( $P_{29}$ ), LT loop mass flow rate ( $\dot{m}_{LT}$ ),  $H_2$  pressure ( $P_{H1}$ ) COM3, and EXP1 outlet pressures ( $P_{N10}$  and  $P_{N2-2}$ ) on the annual thermodynamic, economic, and EI performances of the proposed system when the annual irradiation is set to 5.64 kWh for the desired place.

#### 8.1.1. The effects of pre-cooling section design parameters on the system performances

Figure 5 represents the annual performances of the system with respect to  $P_{21}$ . As  $P_{21}$  ranges from 60 kPa to 140 kPa, the outlet temperature of TUR2 and the inlet temperature of PU2 increase by 4.4% and 8.5%, respectively. These increments lead to greater power production and the reduction of the net consumed power (nearly 4.58%). Therefore,  $COP_{En}$  increased by 4.2%. It can be seen that  $COP_{Ex}$  experienced slight improvements over  $COP_{En}$  because increase in  $P_{21}$  reduced the total exergy destruction of the system by 4.42%, although the produced  $LH_2$  was also reduced by 0.47–0.46 kg/s; consequently, the thermal exergy of  $LH_2$  decreased. Therefore,  $COP_{Ex}$  increased slightly by 1.34%. Moreover, increase of  $P_{21}$  would cause the cost and EI associated with exergy destruction of the overall system to decrease and hence, the cost and EI of  $LH_2$  would be reduced by 4.65–4.11 \$/(kg  $LH_2$ ) and 184.4–176.32 Pts/(kg  $LH_2$ ), respectively.

In Figure 6, a 1.3 kg/s increment in the LT loop mass flow rate caused a decline in the energetic and exergetic performances of the system because the varying mass flow rates decreased the inlet temperature of TUR2 by 7.21% while the outlet temperature was

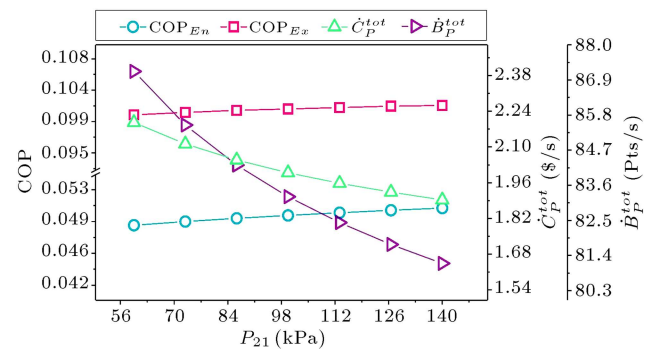


**Figure 5.** Variation of annual performances of the system with  $P_{21}$ .

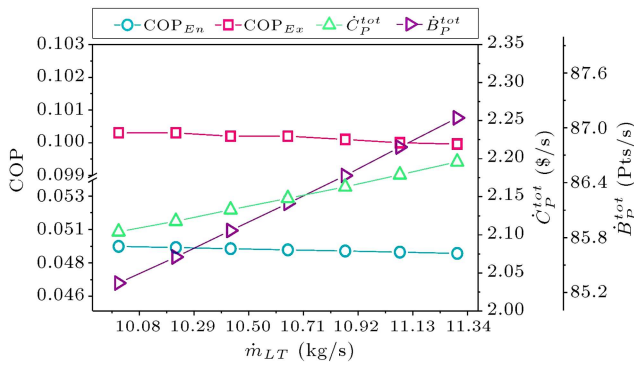


Figure 6. Variation of annual performances of the system with  $\dot{m}_{LT}$ .

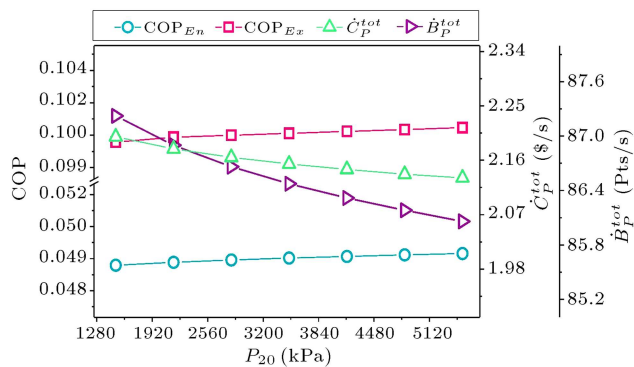


Figure 7. Variation of annual performances of the system with  $P_{20}$ .

reduced by 11.12%; hence, the produced power of TUR2 was enhanced by 2.5%. These reasons cause the increments of consumed power and consequently, the total exergy destruction increase. Thus,  $COP_{En}$  and  $COP_{Ex}$  of the system were reduced by 1.11% and 0.34%, respectively. Due to increases of cost and EI exergy destruction by about 10.8% and 18.45%, the product cost and EI increased by 4.47–4.64 \$/(kg LH<sub>2</sub>) and 181.5–184.4 Pts/(kg LH<sub>2</sub>), respectively. In this case, LH<sub>2</sub> mass flow rate and the consumed power increased slightly by 0.55% and 10.15–10.25 kWh, respectively.

In Figure 7, the variations of system performances with  $P_{20}$  are displayed. Upon an increase in the value of  $P_{20}$  from 1500 kPa to 5500 kPa, the temperature of the pre-cooled H<sub>2</sub> in the solar subsystem was reduced slightly from  $-148.8^{\circ}\text{C}$  to  $-149.3^{\circ}\text{C}$ , and the produced power via TUR2 increased due to the increase in inlet temperature by 7.99%, leading to the reduction of net required power from 10.26 kWh to 10.15 kWh; hence, the annual  $COP_{En}$  increased by 0.9%. Increasing  $P_{20}$  has a slight positive effect on the total exergy destruction of the system by 0.81%. Accordingly, the annual  $COP_{Ex}$  was improved by about 0.76%. Besides, with an increase in  $P_{20}$ , the LH<sub>2</sub> exergy was reduced due to the slight decrement of produced LH<sub>2</sub> (by 0.2%) and both the total cost and EI associated with exergy

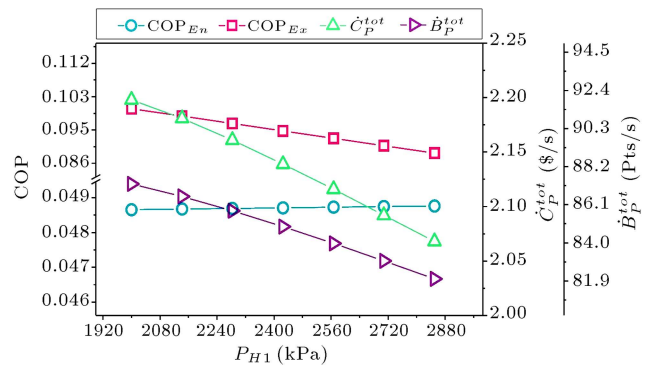


Figure 8. Variation of annual performances of the system with  $P_{H1}$ .

destruction increased by 8.37% and 10.3%, respectively. Therefore,  $\dot{C}_{P,tot}$  the was reduced by 0.07 \$/s, i.e., 0.14 \$/(kg LH<sub>2</sub>), and  $\dot{B}_{P,tot}$  decreased by 1.17 Pts/s, i.e., 2.2 Pts/(kg LH<sub>2</sub>).

8.1.2. The effect of H<sub>2</sub> pressure on the system performances

Figure 8 depicts the influence of  $P_{H1}$  on the annual performances of the system. As can be seen, upon an increase in  $P_{H1}$  from 2000 kPa to 2850 kPa,  $COP_{En}$  increased by 0.28% due to the reduction of the required power. Moreover, the quality of LH<sub>2</sub> increased, which led to quality reduction and also, the reduction of the mass flow rate of LH<sub>2</sub> from 0.47 kg/s to 0.44 kg/s; consequently, the exiting thermal exergy was reduced. On the other hand, the value of total exergy destruction of the system increased by 1% and the net power reduced. These reasons justify the slight increase of  $COP_{En}$  by 0.28% and a decline in  $COP_{Ex}$  by 11.42%. Obviously, both  $\dot{C}_{P,tot}$  and  $\dot{B}_{P,tot}$  were reduced by about 6% due to the decrement of LH<sub>2</sub> exergy. According to the results, increasing  $P_{H1}$  increased the cost and EI of LH<sub>2</sub> by 4.64–4.68 \$/(kg LH<sub>2</sub>) and 184.4–185.7 Pts/(kg LH<sub>2</sub>), respectively.

8.1.3. The effects of MR refrigeration section design parameters on the system performances

Figure 9 shows the effect of  $P_{N10}$  variation on the performances of the system. A 35 kPa increment in  $P_{N10}$  led to slight improvements in  $COP_{En}$  and  $COP_{Ex}$  by 0.33% and 2.06%, respectively, because as PN10 increased, the net power was reduced by 0.368% due to a 0.25% decrement in COM1 required power. In addition, an increase in produced LH<sub>2</sub> from 0.47 kg/s to 0.48 kg/s (36 kg/h) caused the cost and EI rates to increase by 0.5% and 1.25%, while the cost and EI of LH<sub>2</sub> were reduced by 0.06 \$/(kg LH<sub>2</sub>) and 0.82 Pts/(kg LH<sub>2</sub>), respectively. This parameter improved the required power of the system to about 0.44 kWh.

Figure 10 indicates the effect of  $P_{N2-2}$  on the annual performances of the system. Increasing  $P_{N2-2}$  had a negative effect on  $COP_{En}$  and  $COP_{Ex}$  by 1.7%

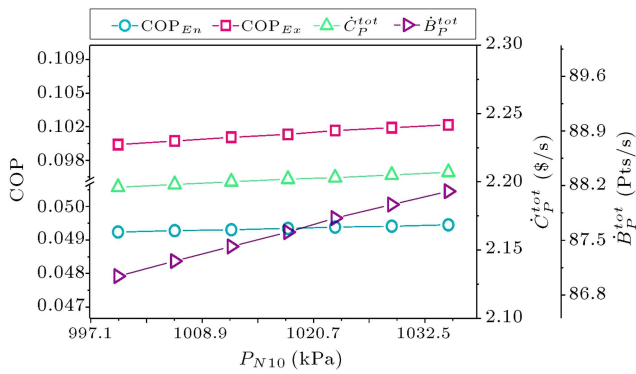


Figure 9. Variation of annual performances of the system with  $P_{N10}$ .

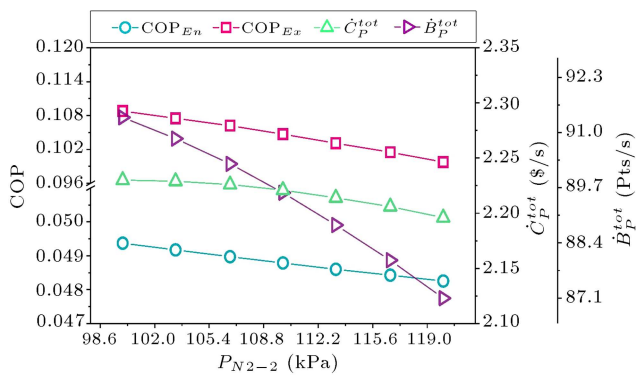


Figure 10. Effects of  $P_{N2-2}$  on system performances.

and 8.31%, respectively, due to a decrement in the power produced by expanders and an increment in the total exergy destruction of the system. The variations of the parameters considerably reduced the amount of produced LH<sub>2</sub> from 0.5 kg/s to 0.47 kg/s. On the other hand, the cost and EI associated with the exergy destruction increased by 11.27% and 8.11%, respectively, which caused the cost and EI rates of the system to reduce, while the produced LH<sub>2</sub> cost and EI increased by 4.41–4.65 \$/(kg LH<sub>2</sub>) and 180.9–184.5 Pts/(kg LH<sub>2</sub>), respectively. Moreover, with an increase in  $P_{N2-2}$ , the value of the required power increased from 10.04 kWh to 10.26 kWh.

### 8.2. Optimization results

According to the parametric study, the same trend can be observed for cost and EI rates of the proposed system. Hence, bi-objective optimization based on NSGA-II was carried out to maximize  $COP_{Ex}$  (Eq. (51)) and minimize  $\dot{B}_P$  (Eq. (54)). In this regard, eight substantial design parameters with the corresponding ranges tabulated in Table 5 were considered as the decision variables. Meanwhile, the genetic algorithm tuning parameters were defined according to the following values: population size 200, migration fraction 0.01, stall generations 100, crossover fraction 0.8, and migration fraction 0.01.

Figure 11 displays the Pareto frontier solution

Table 5. Effective design parameters with the corresponding reasonable ranges.

Parameter	Range
$P_{29}$ (kPa)	740–900
$\dot{m}_{LT}$ (kg/s)	10–11.3
$P_{21}$ (kPa)	59.5–140
$P_{20}$ (kPa)	1500–5500
$P_{H1}$ (kPa)	2000–2850
$P_{N2-2}$ (kPa)	100–120
$P_5$ (kPa)	1500–5050
$P_{N10}$ (kPa)	1000–1035

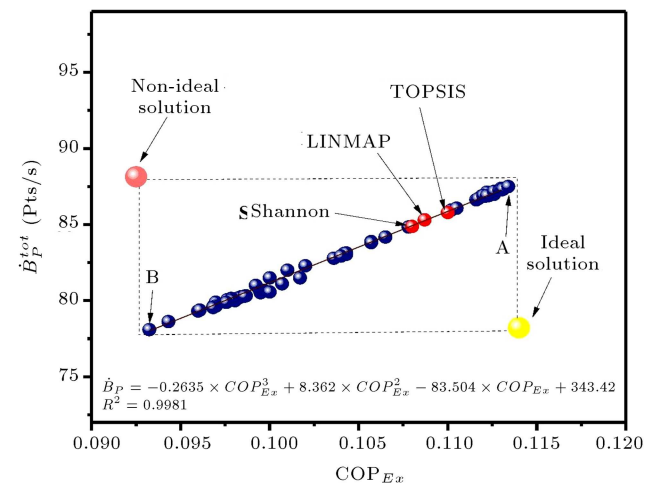


Figure 11. The Pareto frontier optimal distribution for  $COP_{Ex}$  and  $\dot{B}_P$  for the proposed system.

obtained from the optimization, and Table 6 shows detailed parameters of solution points. All points existing in the Pareto frontier can be selected as an optimum solution using decision-makers. As can be seen, there is a clear trade-off between both objectives. The following expression which fitted with the optimized points could provide a suitable relation between  $COP_{Ex}$  and  $\dot{B}_P$  as follows:

$$\dot{B}_P = -0.2635 \times COP_{Ex}^3 + 8.362 \times COP_{Ex}^2 - 83.504 \times COP_{Ex} + 343.42$$

The ideal and non-ideal points shown in Figure 11 obtained using the single-optimization procedure are not located on the Pareto frontier and do not exist in reality. The highest  $COP_{Ex}$  of the system located at point A was estimated as 0.114. This value was equal to that yielded at the ideal point. The worst EI rate and consequently, the cost rate of the system also appeared at point A with the values of 91.74 Pts/s and 2.238 \$/s, respectively. These values were equal to those obtained by single-objective optimization for the non-ideal solution. The proposed system ensured the best

**Table 6.** Bi-objective optimization results for the proposed system.

Point	Decision making method	Decision variables								Objectives			
		$P_{29}$ (kPa)	$\dot{m}_{LT}$ (kg/s)	$P_{21}$ (kPa)	$P_{20}$ (kPa)	$P_{H1}$ (kPa)	$P_{N2-2}$ (kPa)	$P_5$ (kPa)	$P_{PN10}$ (kPa)	$\dot{B}_P$ (Pts/s)	$\dot{C}_P$ (\$/s)	$COP_{Ex}$	$d$
Optimum points	TOPSIS	850	10.01	99.89	5021	2212	100.3	4743	1035	85.79	1.948	0.11	0.3107
	LINMAP	849.2	10.05	100	4897	2300	100.9	4781	1035	85.10	1.935	0.108	0.3443
	Shannon entropy	834.4	10.01	99.77	5014	2300	100	4707	1032	84.87	1.927	0.108	0.3116
A		850	10.01	100	5011	2001	100	2401	1000	91.74	2.238	0.114	–
B		830.3	10.04	100	5041	2697	120	4605	1003	78.13	1.818	0.093	–
Ideal solution		–	–	–	–	–	–	–	–	78.13	1.818	0.114	0
Non-ideal solution		–	–	–	–	–	–	–	–	91.74	2.238	0.093	$\infty$
Base design		735.5	11.32	59.25	1532	2009	119.6	2000	1005	87.20	2.197	0.10	0

$$d = \frac{\sqrt{\sum_{j=1}^n (F_j - F_j^{Ideal})^2}}{\sqrt{\sum_{j=1}^n (F_j - F_j^{Ideal})^2 + \sum_{j=1}^n (F_j - F_j^{Non-ideal})^2}} \tag{43}$$

Box I

values for the EI and cost of the systems by 78.13 Pts/s and 1.818 \$/s, respectively, at point B. The optimum EI and cost rates of the system could be owned at this point using EI rate as the single-objective optimization. Moreover, the lowest  $COP_{Ex}$  could be yielded by 0.093 at point B. Of note, the final optimum point does not possess both maximum  $COP_{Ex}$  and minimum  $\dot{B}_P$ . Therefore, decision-making processes were applied to determine the final optimum solutions using LINMAP, TOPSIS, and Shannon entropy methods. In order to identify the reasonable status of each final optimum point from the ideal one, the deviation index ( $d$ ) is defined by Eq. (43) as shown in Box I [47]. Here,  $F_j$  is the  $j$ th objective function.

According to Table 6, TOPSIS method with the lowest value of  $d$  had the highest reliability among all the other decision-makings. Through this method, the maximum  $COP_{Ex}$  improvement of 10% as well as minimum improvements on  $\dot{C}_P$  and  $\dot{B}_P$  with the values of 11.33% and 1.6%, respectively, could be achieved in comparison to the base design. As observed, Shannon entropy method yielded the highest improvements on  $\dot{C}_P$  and  $\dot{B}_P$  by 12.28% and 2.67%. As can be observed, the final optimum solutions achieved by all decision-making methods were found in the following defined ranges: maximum  $P_{20}$ ,  $P_5$ , and  $P_{N10}$ ; minimum  $\dot{m}_{LT}$ ,  $P_{H1}$ , and  $P_{N2-2}$ ; and in the middle  $P_{29}$  and  $P_{21}$ .

Table 7 lists the characteristics of  $LH_2$  for the optimum solutions obtained using decision-makers. As

can be seen, a 7%  $COP_{Ex}$  improvement to the proposed system was achieved employing TOPSIS and Shannon entropy. The maximum  $LH_2$  mass flow rate of about 4% and the maximum improvements in EI per unit exergy and mass flow rate of  $LH_2$  were obtained by 5.48% and 5.47%, respectively, using TOPSIS method. Outcomes indicated that all decision-makers achieved nearly the same degree of reduction in  $LH_2$  costs by 14.83%.

### 9. Conclusion

A  $H_2$  liquefaction system integrated with Cascade Organic Rankine Cycle (CORC) pre-cooling assisted by solar energy was proposed and analyzed using exergy- and exergy-based concepts. The thermodynamic, economic, and Environmental Impact (EI) performances of the proposed system were assessed over the solstices, equinoxes, and a year for south of Iran. The effects of the main design parameters of CORC and Mixed Refrigerant (MR) cryogenic subsystems on the annual performances of the system were examined. Given the same trend for the cost and EI rates of the system with varying design parameters, the exergetic and EI performances of the system were considered as conflicting objectives in the multi-objective optimization procedure. The optimal solution points were collected as Pareto frontier in which the best solution points were ascertained from exergy and environmental

**Table 7.** LH<sub>2</sub> characteristics for the final optimum solutions.

Parameter	Base design	Decision making method		
		Shannon solution	LINMAP solution	TOPSIS solution
COP <sub>En</sub>	0.05	0.0523	0.0523	0.054
Mass flow rate of LH <sub>2</sub> , $\dot{m}_{LH_2}$ (kg/s)	0.473	0.4861	0.4866	0.4919
Cost per unit exergy of LH <sub>2</sub> , $c_{LH_2}$ (\$/MJ)	0.0363	0.0310	0.0309	0.0309
EI per unit exergy of LH <sub>2</sub> , $b_{LH_2}$ (Pts/MJ)	1.44	1.363	1.362	1.361
Consumed power, $\dot{W}$ (kWh)	10.26	9.52	9.5	9.5
Cost per mass flow rate of LH <sub>2</sub> , $C_{LH_2}$ (\$/kg LH <sub>2</sub> )	4.65	3.96	3.96	3.96
EI per mass flow rate of LH <sub>2</sub> , $B_{LH_2}$ (Pts/kg LH <sub>2</sub> )	184.4	174.61	174.35	174.3

points using LINMAP, TOPSIS, and Shannon entropy decision-makers. The major conclusions of this study may be summarized as follows:

- The average pre-cooled temperature of H<sub>2</sub> in solar CORC reached up to  $-148.8^\circ\text{C}$ , i.e.,  $108.8^\circ\text{C}$  improvement compared with the lowest value reported in the literature;
- In the given design conditions, COP<sub>En</sub> and COP<sub>Ex</sub> were obtained as 0.05 and 0.1. The cost and EI rates of LH<sub>2</sub> were estimated as 0.036 \$/MJ and 1.44 Pts/MJ, respectively;
- The variation tendency of COPs was the opposite of the solar irradiation so that the maximum COP<sub>En</sub> and COP<sub>Ex</sub> were achieved by 0.05 and 0.103, respectively, for February, while the minimum EI of LH<sub>2</sub> was calculated by 184.35 Pts/(kg LH<sub>2</sub>) in this month;
- Results of the parametric study revealed that increasing TUR2 backpressure considerably improved all performances of the proposed system so that COP<sub>En</sub>, COP<sub>Ex</sub> as well as cost and EI of LH<sub>2</sub> exergy unit might be improved by 4.2%, 1.34%, 4.44%, and 11.4%, respectively;
- According to the optimization results, TOPSIS method yielded maximum improvements by 10% and 5.47% for COP<sub>Ex</sub> and EI of LH<sub>2</sub>, respectively, and the highest LH<sub>2</sub> production by 0.4919 kg/s for the proposed H<sub>2</sub> liquefaction system.

**Nomenclature**

$A$	Area, m <sup>2</sup>
$\dot{B}$	Environmental impact rate associated with an exergy stream, Pts/s
$b$	Specific environmental impact per unit of exergy, Pts/kJ
$C$	Concentration ratio

$\dot{C}$	Cost rate associated with an exergy stream, \$/s
$c$	Cost per unit of exergy, \$/kJ
$C_p$	Specific heat of fluid, kJ/kg.K
$D$	Diameter, m
$d$	Deviation index
$\dot{E}_x$	Total exergy rate, kW
$ex$	Specific exergy, kJ/kg
$f$	Coefficient of friction
$f_b$	Exergoenvironmental factor
$f_c$	Exergoeconomic factor
$G_B$	Beam radiation falling on the horizontal surface, kW/m <sup>2</sup>
$h$	Specific enthalpy, kJ/kg
$i_r$	Interest rate, %
$L$	Mirror length, m
$M$	Molecular mass, kg/kmol
$m$	Mass, kg
$\dot{m}$	Mass flow rate, kg/s
$N$	System life, year
$P$	Pressure, kPa
$\dot{Q}$	Heat transfer rate, kW
$Re$	Reynolds number
$r$	Shading factor
$r_b$	Relative environmental impact difference
$r_c$	Relative cost difference
$s$	Specific entropy, kJ/kg.K
$S$	Absorbed solar heat, kW/m <sup>2</sup>
$t$	Time, s
$T$	Temperature, °C
$U$	Overall heat transfer coefficient, kW/m <sup>2</sup> .K
$V$	Velocity, m/s

$w$	Mirror width, m
$\dot{W}$	Power rate, kW
$y$	Molar fraction
$Y$	Component-related environmental impact, Pts
$\dot{Y}$	Component-related environmental impact rate, Pts/s
$Z$	Cost associated with investment expenditures, \$
$\dot{Z}$	Cost associated with investment expenditures, \$/s

### Abbreviation

CHE	Cascade Heat Exchanger
CON	Condenser
CORC	Cascade Organic Rankine Cycle
CRF	Capital Recovery Factor
EI	Environmental Impact
EJC	Ejector
EVP	Evaporator
H <sub>2</sub>	Hydrogen
HE	Heat exchanger
HT	High temperature
LCA	Life Cycle Assessment
LFSC	Linear Fresnel Solar Collector
LH <sub>2</sub>	Liquefied Hydrogen
LT	Low Temperature
MR	Mixed Refrigerant
ORC	Organic Rankine Cycle
PRC	Pre-Cooler Heat Exchanger
PU	Pump
REG	Regenerator
SPECO	Specific Exergy Costing
TST	Thermal Storage Tank
TUR	Turbine
TV	Throttling Valve

### Subscript

0	Dead state
$a$	Air
$amb$	Ambient
$ap$	Aperture
$D$	Destruction
$En$	Energy
$Ex$	Exergy
$f$	Fluid
$F$	Fuel
$g$	Glass cover

$i$	Inner
$inlet$	Inlet
$L$	Loss
$net$	Net
$outlet$	Outlet
$P$	Product
$Q$	Heat transfer
$r$	Receiver
$sun$	Sun
$u$	Useful
$w$	Power

### Superscript

$ch$	Chemical
$CI$	Capital Investment
$M$	Mechanical
$OM$	Operations and Maintenance
$PF$	Pollutant Formation
$Ph$	Physical
$T$	Thermal

### Greek letter

$\alpha$	Absorptivity
$\gamma$	Reflectivity
$\rho$	Density, kg/m <sup>3</sup>
$\tau$	Transitivity
$\eta$	Efficiency, %
$\theta$	Tilt angle, °
$\varphi$	Maintenance factor
$\omega$	Life cycle inventory associated with the production, Pts/kg
$\lambda$	Heat transfer coefficient, kW/m <sup>2</sup> K
$\zeta^0$	Chemical potential in the restricted dead state, kJ/mol
$\zeta^{00}$	Chemical potential in the chemical equilibrium, kJ/mol

### References

1. Krasae-in, S., Stang, J.H., and Neksa, P. "Development of large-scale hydrogen liquefaction processes from 1898 to 2009", *International Journal of Hydrogen Energy*, **35**(10), pp. 4524–4533 (2010).
2. Sadaghiani, M.S. and Mehrpooya, M. "Introducing and energy analysis of a novel cryogenic hydrogen liquefaction process configuration", *International Journal of Hydrogen Energy*, **42**(9), pp. 6033–6050 (2017).
3. Yuksel, Y.E., Ozturk, M., and Dincer, I. "Analysis and assessment of a novel hydrogen liquefaction process", *International Journal of Hydrogen Energy*, **42**(16), pp. 11429–11438 (2017).

4. Stang, J., Neksa, P., and Brendeng, E., *On the Design of an Efficient Hydrogen Liquefaction Process*, in WHEC (2006).
5. Venkatarathnam, G. and Timmerhaus, K., *Cryogenic Mixed Refrigerant Processes*, Springer, **100** (2008).
6. Krasae-In, S., Stang, J.H., and Neksa, P. “Simulation on a proposed large-scale liquid hydrogen plant using a multi-component refrigerant refrigeration system”, *International Journal of Hydrogen Energy*, **35**(22), pp. 12531–12544 (2010).
7. Krasae-in, S., Bredesen, A.M., Stang, J.H., et al. “Simulation and experiment of a hydrogen liquefaction test rig using a multi-component refrigerant refrigeration system”, *International Journal of Hydrogen Energy*, **36**(1), pp. 907–919 (2011).
8. Krasae-in, S. “Optimal operation of a large-scale liquid hydrogen plant utilizing mixed fluid refrigeration system”, *International Journal of Hydrogen Energy*, **39**(13), pp. 7015–7029 (2014).
9. Kuendig, A., Loehlein, K., Kramer, G.J., et al. “Large scale hydrogen liquefaction in combination with LNG re-gasification”, in *Proceedings of the 16th World Hydrogen Energy Conference*, Lyon, France (2006).
10. Kanoglu, M., Bolatturk, A., and Yilmaz, C. “Thermodynamic analysis of models used in hydrogen production by geothermal energy”, *International Journal of Hydrogen Energy*, **35**(16), pp. 8783–8791 (2010).
11. Gadalla, M.A., Ratlamwala, T.A.H., Dincer, I., et al. “Performance assessment of an integrated absorption cooling-hydrogen liquefaction system using geothermal energy”, *International Journal of Exergy*, **12**(2), pp. 205–225 (2013).
12. Kanoglu, M., Yilmaz, C., and Abusoglu, A. “Geothermal energy use in absorption precooling for Claude hydrogen liquefaction cycle”, *International Journal of Hydrogen Energy*, **41**(26), pp. 11185–11200 (2016).
13. Yilmaz, C. “A case study: Exergoeconomic analysis and genetic algorithm optimization of performance of a hydrogen liquefaction cycle assisted by geothermal absorption precooling cycle”, *Renewable Energy*, **128**, pp. 68–80 (2018).
14. Aasadnia, M. and Mehrpooya, M. “Conceptual design and analysis of a novel process for hydrogen liquefaction assisted by absorption precooling system”, *Journal of Cleaner Production*, **205**, pp. 565–588 (2018).
15. Wang, X., Zhao, L., Wang, J.L., et al. “Performance evaluation of a low-temperature solar rankine cycle system utilizing R245fa”, *Solar Energy*, **84**(3), pp. 353–364 (2010).
16. Gang, P., Jing, L., and Jie, J. “Design and analysis of a novel low-temperature solar thermal electric system with two-stage collectors and heat storage units”, *Renewable Energy*, **36**(9), pp. 2324–2333 (2011).
17. Li, J., Pei, G., Li, Y., et al. “Energetic and exergetic investigation of an organic Rankine cycle at different heat source temperatures”, *Energy*, **38**(1), pp. 85–95 (2012).
18. Kaşka, Ö., Yilmaz, C., Bor, O., et al. “The performance assessment of a combined organic Rankine-vapor compression refrigeration cycle aided hydrogen liquefaction”, *International Journal of Hydrogen Energy*, **43**(44), pp. 20192–20202 (2018).
19. El Gharbi, N., Derbal, H., Bouaichaoui, S., et al. “A comparative study between parabolic trough collector and linear Fresnel reflector technologies”, *Energy Procedia*, **6**, pp. 565–572 (2011).
20. Häberle, A., Zahler, C., Lerchenmüller, H., et al. “The solarmundo line focusing fresnel collector. Optical and thermal performance and cost calculations”, in *Proceedings of the International Symposium on Concentrated Solar Power and Chemical Energy Technologies*, SolarPACES, Zürich, Sep. (2002).
21. Hu, E.J., Mills, D.R., Morrison, G.L., et al. “Solar power boosting of fossil fuelled power plants”, in *Proceedings of the International Solar Energy Congress* (2003).
22. Abbas, R., Montes, M.J., Piera, M., et al. “Solar radiation concentration features in linear Fresnel reflector arrays”, *Energy Conversion and Management*, **54**(1), pp. 133–144 (2012).
23. Calm, J.M. and Hourahan, G.C. “Physical, safety, and environmental data for current and alternative refrigerants”, in *Proceedings of 23rd International Congress of Refrigeration (ICR2011)*, Prague, Czech Republic, August (2011).
24. Xue, X., Guo, C., Du, X., et al. “Thermodynamic analysis and optimization of a two-stage organic rankine cycle for liquefied natural gas cryogenic exergy recovery”, *Energy*, **83**, pp. 778–787 (2015).
25. Bolaji, B.O. “Selection of environment-friendly refrigerants and the current alternatives in vapour compression refrigeration systems”, *Environmental Science*, **1**(1), pp. 22–26 (2011).
26. Wang, M., Wang, J., Zhao, P., et al. “Multi-objective optimization of a combined cooling, heating and power system driven by solar energy”, *Energy Conversion and Management*, **89**, pp. 289–297 (2015).
27. Li, H. Cao, F., Bu, X., et al. “Performance characteristics of R1234yf ejector-expansion refrigeration cycle”, *Applied Energy*, **121**, pp. 96–103 (2014).
28. Boyaghchi, F.A. and Sohbatloo, A. “Assessment and optimization of a novel solar driven natural gas liquefaction based on cascade ORC integrated with linear Fresnel collectors”, *Energy Conversion and Management*, **162**, pp. 77–89 (2018).
29. Reddy, V.S., Kaushik, S., and Tyagi, S. “Exergetic analysis of solar concentrator aided natural gas fired combined cycle power plant”, *Renewable Energy*, **39**(1), pp. 114–125 (2012).
30. Bejan, A. and Tsatsaronis, G., *Thermal Design and Optimization*, John Wiley & Sons (1996).
31. Kotas, T.J., *The Exergy Method of Thermal Plant Analysis*, Elsevier (2013).

32. Tsatsaronis, G. “Definitions and nomenclature in exergy analysis and exergoeconomics”, *Energy*, **32**(4), pp. 249–253 (2007).
33. Syed, M., Sherif, S.A., Veziroglu, T.N., et al. “An economic analysis of three hydrogen liquefaction systems”, *International Journal of Hydrogen Energy*, **23**(7), pp. 565–576 (1998).
34. Ansarinassab, H., Mehrpooya, M., and Sadeghzadeh, M. “An exergy-based investigation on hydrogen liquefaction plant-exergy, exergoeconomic, and exergoenvironmental analyses”, *Journal of Cleaner Production*, **210**, pp. 530–541 (2019).
35. Boyaghchi, F.A., Chavoshi, M., and Sabeti, V. “Optimization of a novel combined cooling, heating and power cycle driven by geothermal and solar energies using the water/CuO (copper oxide) nanofluid”, *Energy*, **91**, pp. 685–699 (2015).
36. Boyaghchi, F.A. and Chavoshi, M. “Monthly assessments of exergetic, economic and environmental criteria and optimization of a solar micro-CCHP based on DORC”, *Solar Energy*, **166**, pp. 351–370 (2018).
37. Meyer, L., Tsatsaronis, G., Buchgeister, J., et al. “Exergoenvironmental analysis for evaluation of the environmental impact of energy conversion systems”, *Energy*, **34**(1), pp. 75–89 (2009).
38. Morosuk, T., Tsatsaronis, G., and Koroneos, C. “Environmental impact reduction using exergy-based methods”, *Journal of Cleaner Production*, **118**, pp. 118–123 (2016).
39. Cavalcanti, E.J.C. “Exergoeconomic and exergoenvironmental analyses of an integrated solar combined cycle system”, *Renewable and Sustainable Energy Reviews*, **67**, pp. 507–519 (2017).
40. Morosuk, T. and Tsatsaronis, G. “Exergoenvironmental analysis is a new tool for evaluation of an energy conversion system”, **4**, pp. 3–14 (2013).
41. Petrakopoulou, F., Tsatsaronis, G., Morosuk, T., et al. “Environmental evaluation of a power plant using conventional and advanced exergy-based methods”, *Energy*, **45**(1), pp. 23–30 (2012).
42. Morosuk, T., Tesch, S., Hiemann, A., et al. “Evaluation of the PRICO liquefaction process using exergy-based methods”, *Journal of Natural Gas Science and Engineering*, **27**, pp. 23–31 (2015).
43. Van Gool, W., *Energy Policy: Fairy Tales and Factualities, in Innovation and Technology-Strategies and Policies*, Springer, pp. 93–105 (1997).
44. Deb, K., Pratap, A., Agarwal, S., et al. “A fast and elitist multiobjective genetic algorithm: NSGA-II”, *IEEE Transactions on Evolutionary Computation*, **6**(2), pp. 182–197 (2002).
45. Zitzler, E., Deb, K., and Thiele, L. “Comparison of multiobjective evolutionary algorithms: Empirical results”, *Evolutionary Computation*, **8**(2), pp. 173–195 (2000).
46. Sadeghi, M., Yari, M., Mahmoudi, S.M.S., et al. “Thermodynamic analysis and optimization of a novel combined power and ejector refrigeration cycle-desalination system”, *Applied Energy*, **208**, pp. 239–251 (2017).
47. Li, Y., Liao, S., and Liu, G. “Thermo-economic multi-objective optimization for a solar-dish Brayton system using NSGA-II and decision making”, *International Journal of Electrical Power & Energy Systems*, **64**, pp. 167–175 (2015).

## Biographies

**Fateme Ahmadi Boyaghchi** is an Associate Professor of Mechanical Engineering at Alzahra University, Tehran, Iran. She received her PhD in 2011 from IUST, Iran. Her research interests include renewable energy systems, exergy-based methods, and optimization.

**Arezoo Sohbatloo** received her MSc degree in Energy Systems Engineering from Alzahra University and her BS degree in Mechanical Engineering from Zanjan University. Her expertise is solar energy systems with focus on sensitivity analysis and optimization.